Magnetic Structures of Mn 11 Ta 4 O 21 and Interpretation as an Hexagonal A-site Manganite

Cintli Aguilar-Maldonado, Eugenia Arévalo-López, Clemens Ritter, Olivier Mentré, Angel Arévalo-López

Magnetic structures of $Mn_{11}Ta_4O_{21}$ and interpretation as an hexagonal A-site manganite.

Cintli Aguilar-Maldonado[a], Eugenia P. Arévalo-López[b], Clemens Ritter[c], Olivier Mentré[a], Ángel M. Arévalo-López[a]*

[a] Univ. Lille, CNRS, Centrale Lille, Univ. Artois, UMR 8181 – UCCS – Unité de Catalyse et Chimie du Solide, F-59000 Lille, France.

[b] Física Atómica y Molecular, Facultad de Ciencias, UNAM. Ciudad Universitaria, A.P. 70-399, Ciudad de México, 04510, México.

[c] Institut Laue-Langevin, 71 Avenue des Martyrs, 38042, Grenoble Cedex, France. * angel.arevalo-lopez@univ-lille.fr

ABSTRACT: $Mn_{11}Ta_4O_{21}$ is presented as the first Hexagonal A-site Manganite. Based on simple rules, the structure is compatible with a 14H-layer $(cchchch)_2$ stacking sequence; related to $BaVO_3$ and $BaCrO_3$ high pressure polymorphs. The A-site over-stoichiometry is explained through difference in ionic radii sizes between Ba and Mn. Magnetic properties show two transitions at T_{N1} = 88 K and T_{N2} = 56 K. Neutron powder diffraction evidence two magnetic structures with purely antiferromagnetic and ferrimagnetic orders below T_{N1} and T_{N2} respectively. A complementary description with 14H-$(hhccccc)_2$ sequence of only Mn octahedra provides a direct comparison with $BaMnO_{3-\delta}$ hexagonal perovskites and naturally explains the AFM order. Below T_{N2} a magneto-elastic coupling along with uniaxial negative thermal expansion are observed.

Introduction

ABO_3 oxide perovskites are amongst the most studied materials due to their structural, chemical and physical properties versatility associated with a diversified field of applications. Besides the most commonly admitted cubic (*c*) – based 3C (*e.g.* $SrCrO_3$) (1) stacking sequence of AO_3 layers, hexagonal perovskites show a mixture of (*c*) and hexagonal (*h*) stackings, with the end member being the 2H $(h)_2$ (*e.g.* $BaNiO_3$) polytype (2).

In recent years, the incorporation of Mn^{2+} into the A-site of perovskites has gained interest due to the allowance of complex electronic and magnetic A-B interactions. For example, the spintronic material $Mn^{2+}V^{4+}O_3$ with localized and magnetically ordered Mn^{2+} $3d^5$ and itinerant V^{4+} $3d^1$ electrons (3). Several $Mn_2BB'O_6$ double perovskites and corundum related structures have also been obtained with Mn^{2+} at the A-site (4-7). However, all of these A-site manganite phases require the use of high pressure – high temperature synthesis techniques which restricts somehow the available amounts of sample. It is therefore appealing to search for more easily synthesized analogues where Mn is found on the A-site.

Regarding the MnO-Ta_2O_5 system, different stoichiometries have been obtained via solid state routes, $Mn_4Ta_2O_9$, $Mn_3Ta_2O_8$, $MnTa_2O_6$ and $Mn_{11}Ta_4O_{21}$ are the most notorious ones. From those, only the first two have been properly characterised, with multiferroic and optical properties respectively (8-11).

$Mn_{11}Ta_4O_{21}$ possesses a structure which has previously been described as consisting of alternating $Mn_4Ta_2O_6$ and MnO layers and it shows a well-defined maximum at 23 K in the magnetic susceptibility (11). In this paper, we re-examine in more detail the $Mn_{11}Ta_4O_{21}$ oxide and show how it can be described as a 14H-layer hexagonal perovskite, making it the first Hexagonal A-site Manganite (HAM). It can be synthesised by conventional solid-state methods, lifting the restriction of small quantities from high-pressure A-site manganites. Magnetic susceptibility measurements and neutron diffraction show two magnetic transitions which correspond to a spin reorientation from an antiferromagnet to a ferrimagnet with a 2 μ_B remnant magnetisation at low temperatures.

Experimental

Stoichiometric amounts of MnO and Ta_2O_5 (Alfa Aesar) were mixed in an agate mortar, pelletized and sealed into a quartz ampoule. The pellets were heated to 900 °C for 12 hours, ground, pelletized, sealed and heated again. A small amount of $Mn_4Ta_2O_9$ was detected (<10%) and considered in the interpretation of our results.

X-ray diffraction (XRD) was performed on a Cu-$K_{\alpha 1}$ Bruker D8 Advance diffractometer on a Bragg-Brentano geometry in the $5 < 2\theta < 90^o$ range. Synchrotron XRD were collected at room temperature using the BL04 beamline at ALBA, Barcelona (λ = 0.412845 Å). Neutron powder diffraction (NPD) data were taken between 1.5 and 120 K every 10 K using the D1B beamline at the ILL, Grenoble (λ = 2.52 Å).

Magnetic measurements were performed on a Physical Properties Measurement System (PPMS) Dynacool (9T) system from Quantum Design. Zero field cooling (ZFC) and field cooling (FC) procedures between 2 < T < 300 K under a 0.1 T magnetic field and magnetization versus field between -9 and 9 T at various temperatures were measured. Dielectric properties were measured using an Agilent E4980A LCR meter. Electrodes were prepared on the sample with silver paste on the planar surfaces.

Rietveld refinement was done with Fullprof Suite; magnetic symmetry analysis was performed using the program BasIreps implemented in the same software (12). Mode analysis was made with the ISODISTORT internet-based tool (13,14).

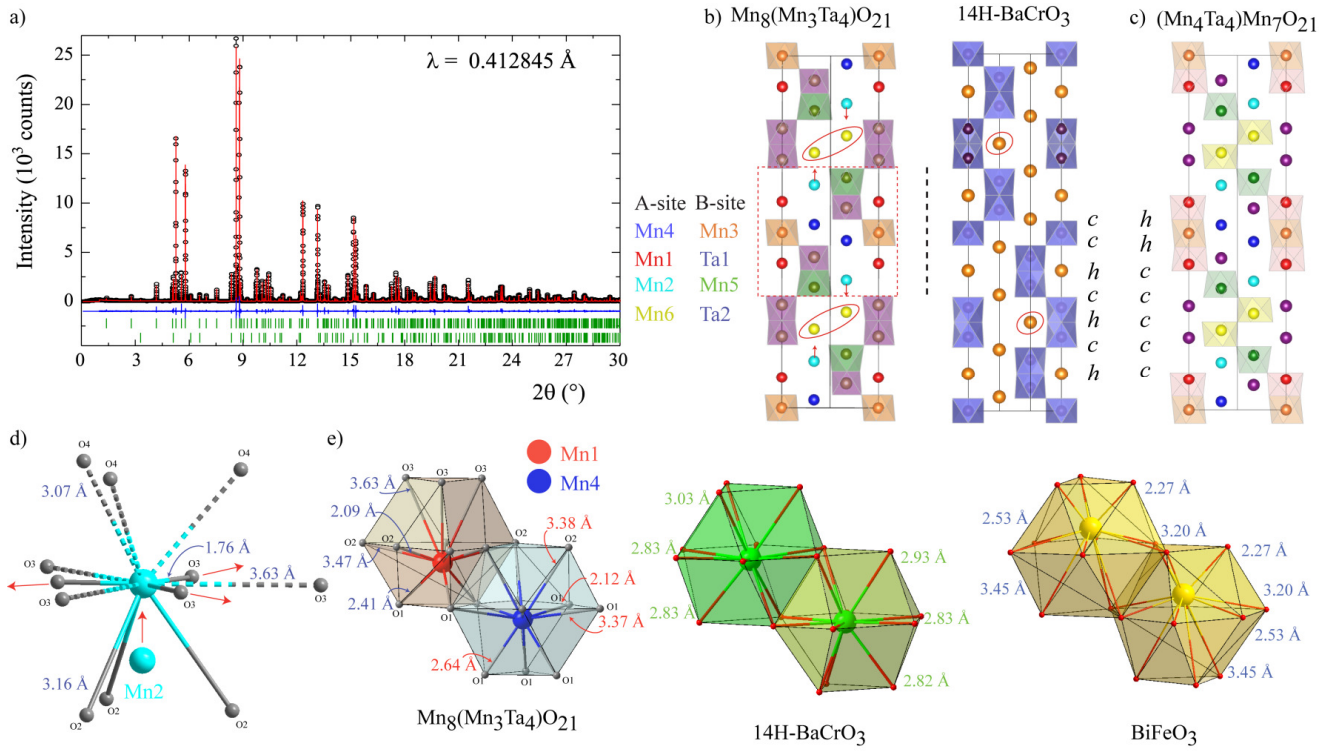

Figure 1. a) Rietveld fit of the $Mn_{11}Ta_4O_{21}$ compound from 300 K SXRD data. Second row of Bragg tick marks corresponds to the $Mn_4Ta_2O_9$ minority phase. b) $Mn_{11}Ta_4O_{21}$ crystal structure compared with 14H-$BaCrO_3$ showing A- and B-site selections. Only the TaO_6 and the less-distorted MnO_6 octahedra are drawn, see the text. Red ellipses show the 2Mn6 – 1Ba equivalence. Red dotted square remarks the mirror-reflection twinned section of the $Mn_{11}Ta_4O_{21}$ structure respects to the 14H-$BaCrO_3$. c) Different stacking sequence, with only MnO_6 octahedra, see text. d) Ideal coordination around Mn2 with argued displacements marked with red arrows. e) A-site comparison for Mn1 and Mn4 with equivalent sites in the 14H-$BaCrO_3$ and $BiFeO_3$.

Table 1. Atomic positions, isotropic and anisotropic thermal displacement parameters and BVS calculations obtained from the Rietveld fit of 300 K SXRD data. S.G. *P-3c1*, *a* = 5.37852(2) Å, *c* = 34.02833(13) Å.

Site	x	y	z	B iso*	U11 (Å²)*	U33 (Å²)*	BVS
Mn1 (4c)	0.00000	0.00000	0.08706(9)	--	0.002(1)	0.003(2)	1.89(2)
Mn2 (4d)	0.66666	0.33333	0.1350(2)	--	0.014(2)	0.023(4)	1.90(2)
Mn3 (2b)	0.00000	0.00000	0.00000	--	0.007(2)	0.012(4)	2.01(3)
Mn4 (4d)	0.33333	0.66666	0.9766(2)	--	0.012(2)	0.073(4)	1.55(3)
Mn5 (4d)	0.33333	0.66666	0.1558(1)	--	0.002(1)	0.003(1)	1.98(3)
Mn6 (4d)	0.66666	0.33333	0.2264(1)	--	0.002(1)	0.002(1)	1.85(2)
Ta1 (4d)	0.33333	0.66666	0.07013(5)	--	0.0071(5)	0.0057(8)	5.51(7)
Ta2 (4d)	0.00000	0.00000	0.20517(3)	--	0.0074(5)	0.0076(8)	5.21(7)
O1 (4c)	0.648(2)	0.705(3)	0.0385(2)	0.5(3)	--	--	-2.02(4)
O2 (12g)	0.349(2)	0.388(2)	0.1062(3)	0.3(2)	--	--	-1.98(3)
O3 (12g)	0.698(3)	0.675(1)	0.1814(3)	0.7(2)	--	--	-1.98(3)
O4 (6f)	0.270(2)	0.270(2)	0.25000	0.9(3)	--	--	-1.98(2)

* U_{ij} symmetry constrains: U11 = U22, U12 = 0.5U11, U13 = U23 =0. Rp = 0.11, Rexp = 0.14, χ^2 = 1.13.

Results and discussion

Figure 1a shows the Rietveld fit of $Mn_{11}Ta_4O_{21}$ for SXRD at 300 K. As previously reported (11)[Erreur ! Signet non défini.], $Mn_{11}Ta_4O_{21}$ crystallises in the space group *P*-3*c*1 (No. 165) with a = 5.3782(1) Å and c = 34.0256(2) Å. Refinement results along with, bond distances, angles and the octahedral distortion defined as $\Delta_d = (1/6)\Sigma_{n=1-6}[(d_n - <d>/<d>]^2$ (15) are summarised in Tables 1 and 2 and the structure is shown in Figure 1b. Mn/Ta sites are fully ordered and consist of six independent Mn and two Ta surrounded by O atoms. The Mn-O distances range from 2.065(1) to 2.603(4) Å and the Ta-O between 1.899(1) and 2.120(1) Å. Bond valence sum calculations for Mn and Ta are very close to the +2 and +5 expected values except for the face sharing Mn4 (1.6+) and Ta1 (5.5+) which highlights the atomic stress in the structure. Δ_d values in Table 1 show that within the manganese octahedra $Mn3O_6$ (point group symmetry $\bar{3}$), $Mn5O_6$ and $Mn6O_6$ are the less distorted, while $Mn4O_6$ is strongly stressed as Mn4 is off-centered by 0.79 Å from its octahedra (D parameter in Table 2). In Figure 1b the structure is drawn in a representation which highlights the similarity with the hexagonal 14H-type obtained from high-pressure synthesis observed for $BaVO_3$ (16) and $BaCrO_3$ (17) with a $(cchchch)_2$ stacking sequence, see Figure 1b and c. Only one octahedral is drawn at each layer height for $Mn_{11}Ta_4O_{21}$ (Figure 1b, left): Either a TaO_6 or the less distorted MnO_6 when only manganese is present in the layer, *i.e.* $Mn3O_6$ and $Mn5O_6$ *vs.* $Mn4O_6$ and $Mn2O_6$. The two main differences with the 14H-sequence of $BaVO_3$ and $BaCrO_3$ stem from an over-stoichiometry on the A-site, resulting in $Mn_8(Mn_3Ta_4)O_{21}$, which is accounted for on the Mn6 site and marked with a red ellipse in Figure 1b (left) and its stoichiometric equivalent in Figure 1b (right). This A-site over stoichiometry is not so un-common, observed as well for instance in the parent compound $Ca_3Co_2O_6$ and in the full series of hexagonal perovskite related $A_{1+x}BO_3$ compounds built on prismatic/octahedral columns (18). In this series the equivalent stoichiometric form would be the 2H hexagonal perovskite *e.g.* $BaNiO_3$, with 1D chains as distinctive motifs. Therefore, in the present case, a more suitable formulation would be $A_{(n+1)}B_nO_{3n}$ with n = 7.

The second difference between the two sequences is seen when using a modular description where a mirror-reflection twinning operation (broken-black line in Figure 1b) acting on a third of the structure (red rectangle in Figure 1b) is needed to transform one structure into the other (19). This tectonic approach resembles the EMMA method for building functional inorganic materials where the stacking of blocks would dictate the functional or multifunctional (by assembly) properties of the material (20). In here, Mn4, the central atom at the twinned block, modifies drastically the structure and the magnetic properties as described below.

In the ideal case, without Mn4 over-stoichiometry, Mn2 would be displaced towards a more A-site type coordination through a typical "push and pull" scenario" as depicted in Fig.1d. As mentioned before, Mn1 and Mn4 are the most distorted octahedra and they are the most related to the A-site in perovskites. Figure 1e) shows the comparison with the equivalent A-site in 14H-$BaCrO_3$ and $BiFeO_3$, one of the most studied multiferroic perovskites. The similarity in the icosahedral coordination can clearly be seen The Mn-O bond distances to this A-site type coordination go up 3.628(8) Å as detailed in Table 2. This distance is not so far from the 3.45 Å for Bi-O bonds in $BiFeO_3$. Moreover, the icosahedral square-face sharing between Mn1 and Mn4 is also observed in 14H-$BaCrO_3$ and $BiFeO_3$. However, the displacement from the oxygen from its ideal position in a compact type allows several stacking sequences as detailed later.

Table 2. Selected bond and metal-metal distances and angles, octahedral distortions (Δ_d) and displacement from barycentre (D) for $Mn_{11}Ta_4O_{21}$ at 300K. The subscript in the average indicates the number of bonds used.

d_{M-O}	(Å)	d_{M-O}	(Å)
3x (Mn1-O1)	2.414(8)	3x (Mn2-O2)	2.11(1)
3x (Mn1-O2)	2.092(8)	3x (Mn2-O3)	2.36(1)
$<Mn1 - O>_6$	2.252(4)	$< Mn2 - O>_6$	2.236(5)
3x (Mn1-O1)	3.628(8)	6x (Mn3-O1)	2.194(8)
3x (Mn1-O2)	3.466(8)	$< Mn3 - O>_6$	2.194(8)
$<Mn1 - O>_{12}$	2.899(4)	3x (Mn6-O3)	2.33(1)
3x (Mn4-O1)	2.64(1)	3x (Mn6-O4)	2.142(7)
3x (Mn4-O1)	2.11(2)	$< Mn6 - O>_6$	2.236(5)
$< Mn4 - O>_6$	2.379(5)	3x (Ta1-O1)	1.93(1)
3x (Mn4-O1)	3.37(2)	3x (Ta1-O2)	1.98(1)
3x (Mn4-O1)	3.38(1)	$< Ta1 - O>_6$	1.952(5)
$< Mn4 - O>_{12}$	2.875(5)	3x (Ta2-O3)	1.874(8)
3x (Mn5-O2)	2.12(2)	3x (Ta2-O4)	2.106(9)
3x (Mn5-O3)	2.29(1)	$< Ta2 - O>_6$	1.990(4)
$< Mn5 - O>_6$	2.209(5)		
M-O-M	(°)	**M-O-M**	(°)
Mn1-O1-Mn3	79.9(3)	Mn3-O1-Ta1	143.6(4)
Mn1-O1-Ta1	92.6(4)	Mn4-O1-Ta1	86.7(3)
Mn1-O2-Mn2	113.3(5)	Mn4-O1-Ta1	119.3(4)
Mn1-O2-Ta1	101.7(5)	Mn5-O2-Ta1	85.8(2)
Mn1-O1-Mn4	113.3(3)	Mn5-O3-Mn2	90.2(4)
Mn2-O3-Ta2	134.9(4)	Mn5-O3-Mn6	123.4(3)
Mn2-O2-Mn5	92.7(4)	Mn5-O2-Mn1	124.9(5)
Mn2-O3-Mn5	92.0(5)	Mn5-O3-Ta2	123.8(6)
Mn2-O3-Mn6	83.0(3)	Mn6-O4-Mn6	109.4(6)
Mn2-O2-Ta1	137.5(3)	Mn6-O4-Ta2	132.1(3)
Mn3-O1-Mn4	96.2(5)	Mn6-O3-Ta2	98.0(3)
Mn3-O1-Mn4	82.4(2)	Ta2-O4-Ta2	92.8(2)
M -M	**(Å)**	**M -M**	**(Å)**
Mn1 – Mn3	2.962(3)	Mn4 – Ta1	3.181(6)
Mn1 – Ta1	3.1582(7)	Mn5 – Ta1	2.914(5)
Mn2 – Mn6	3.109(7)	Mn6 – Ta2	3.1880(9)
Mn2 – Mn5	3.185(2)	Ta2 – Ta2	3.051(2)
Mn3 – Mn4	3.205(1)		

	Δ_d x 10^{4*}	D (Å)		Δ_d x 10^{4*}	D (Å)
Mn1	51.0	0.50	Mn5	14.2	0.41
Mn2	31.4	0.30	Mn6	18.0	0.36
Mn3	0	0	Ta1	1.6	0.08
Mn4	126.2	0.79	Ta2	34.1	0.36

*Octahedral distortions calculated from $\Delta_d=(1/6)*\Sigma(d_i-d_{av})^2/d_{av}$.

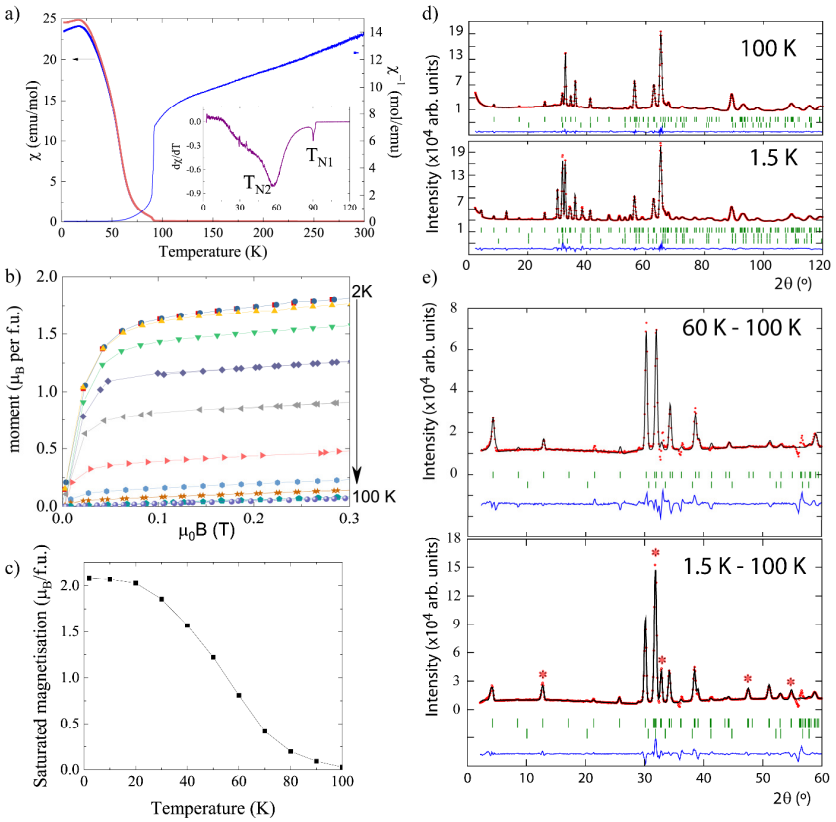

Figure 2. a) ZFC (blue) and FC (red) magnetic susceptibility of $Mn_{11}Ta_4O_9$ (left axis). Inverse susceptibility is shown on the right axis and the derivative in the inset with the two transitions marked. b) Field dependent magnetisation curves at different temperatures. c) Saturated magnetisation obtained from linear fits from 5 T to 9 T of data from b). d) Rietveld of the nuclear and magnetic structures to the 100 K (top) and 1.5 K (bottom) NPD data of $Mn_{11}Ta_4O_{21}$. e) Rietveld fit of the magnetic model to the 60 K – 100 K (top) and 1.5 K – 100 K (bottom) difference patterns. Asterisks show the most prominent changes in magnetic intensity from 60 K to 1.5 K. The second row of Bragg tick marks corresponds to the $Mn_4Ta_2O_9$ secondary phase crystal and magnetic structures.

The ZFC and FC magnetic susceptibilities of $Mn_{11}Ta_4O_{21}$ were measured under a 250 Oe external field (Figure 2a-top). A sharp antiferromagnetic (AFM) magnetic transition is observed at T_{N1} = 88 K. The derivative ($d\chi/dT$, inset Figure 2a) shows a second transition at T_{N2} = 56 K where also a ferromagnetic component is implied by the ZFC – FC divergence. Curie-Weiss fit to the inverse of susceptibility above 125 K gives μ_{eff} = 5.42 μ_B/Mn, close to the expected value of 5.92 μ_B for spin only Mn^{2+} (S = 5/2). The negative Weiss constant θ = - 248(1) K shows predominant AFM interactions. However, magnetisation curves under applied field at different temperatures (Figure 2a-bottom) show field induced correlations below T_{N1} with a probable origin from disordered spins in Mn4 as detailed later. Just below T_{N2} a clear ferrimagnetic contribution appears with a 2 μ_B per f.u. (formula unit) remnant magnetisation at 2 K. The resulting moment observed in magnetisation curves below T_{N2} comes from an imbalance between different Mn spin components as later described.

Rietveld refinements to NPD collected at 100 K and 1.5 K are shown in Figure 2b. These confirmed the well-ordered distribution between Mn and Ta due to the large difference in neutron scattering lengths (-3.73/6.91 fm for Mn/Ta). Magnetic diffraction peaks appear below T_{N1} and were indexed with a k = [0 0 0] propagation vector (Γ point of the first Brillouin zone). Since the structure contains six independent Mn sites, initial magnetic symmetry analysis performed with BasIreps tool in Fullprof Suite (12) and the subsequent trial refinements were unsuccessful. However, a different approach with a full magnetic space group description obtained from the ISODISTORT web-based tool (13) was adopted and two subsequent magnetic structures have been discovered in $Mn_{11}Ta_4O_{21}$. Below 90 K and in accordance with magnetic susceptibility measurements, magnetic intensity is observed in the NPD data. The best fit to the 60 K NPD data was obtained with the mΓ3+ irreducible representation in a {(2, 1, 0), (0, 1, 0), (0, 0, 1)} pseudo-orthorhombic supercell with the monoclinic *C2′/c′* magnetic space group (15.89) as shown in Figure 2e top and Supplementary Figure 1. This high temperature magnetic structure can be described as FM layers (with Mn2 and Mn5 in the same layer) coupled AFM along the *c* direction with idle Mn4, but ordered spins for the rest of the Mn cations along the *y* axis in the pseudo-orthorhombic cell (see Figure 3). Below 60 K, extra magnetic contribution grows, as shown in Figure 3d. The low temperature magnetic structure differs from the previous by the activation of a FM complementary mode in the same mΓ3+ irreducible representation and implies a spin reorientation; note that mΓ2+ is present as second order parameter (i.e. it is not sufficient to reduce the symmetry but is still present in the transition). mΓ2+ implies FM ordering along the *c* direction and it was tested as a possible trigger for the transition at T_{N2}, however following a 3σ criterion (i.e. mode amplitudes < 3σ were fixed to zero)

we can conclude that the only responsible for the transition is mΓ3+. Mn1, Mn2, Mn3 and Mn4 develop a m_x spin component. Mn5 and Mn6 moments were constrained to be antiparallel along the whole temperature range and release of this constrain result in unstable refinements and unphysically high moments for Mn5 and Mn6. The refinement from a 1.5 K – 100 K difference pattern is shown in Figure 2e bottom. Figure 3c shows the behaviour of the Mn moments and the angle φ with the *x* axis. The moments converge to 4.3(3), 3.1(2), 3.8(2), 2.7(3), 4.0(3) μ_B for Mn1, Mn2, Mn3, Mn4 and Mn5(Mn6) at 1.5 K. Obviously, the resulting moment observed in magnetisation curves below T_{N2} comes from an imbalance between different Mn-m_x. The resultant ferrimagnetic moment at 1.5 K from NPD is m_x = -0.7(1) μ_B, which accounts for the moment observed in the magnetic hysteresis loops after alignment in Figure 2b. Figure 2c shows the saturated moment above 5 T extrapolated to B = 0 with a clear increase below 60 K.

Table 3. m_x and m_y refined moment components at 60 K (top) and 1.5 K (bottom), m_z = 0 for all atoms. Total moment and φ angle. ABO_3 assignment is based in $(hhcccc)_2$ stacking sequence.

	ABO_3 site in $(hhcccc)_2$	m_x (μ_B)	m_y (μ_B)	mTot (μ_B)	φ (°)
Mn1	B	0	3.2(2)	3.2(2)	90
		1.4(1)	4.0(3)	4.3(3)	48(3)
Mn2	A	0	1.2(2)	1.2(2)	90
		-2.7(2)	-1.6(1)	-3.1(2)	31(2)
Mn3	B	0	-2.5(2)	-2.5(2)	90
		2.7(2)	-2.6(2)	3.8(2)	-45(4)
Mn4	A	0	0.0(2)	0.0(2)	--
		-2.7(3)	0	-2.7(3)	0
Mn5*	B	0	-3.2(2)	-3.2(2)	90
		0	-4.0(3)	-4.0(3)	90
Mn6*	B	0	3.2	3.2	90
		0	4.0	4.0	90

* Constrained together to be antiparallel.

The thermal evolution of the cell parameters in the magnetically ordered state are shown in Figure 4a. They were refined in the pseudo-orthorhombic magnetic cell and show no significant deviation from the hexagonal cell *i.e.* $a \approx b/\sqrt{3}$. Below T_{N2} = 56 K a uniaxial negative thermal expansion develops along the *c* direction, implying that the FM interactions are frustrated, i.e. the lattice expands to relief this frustration maximizing the distance between the different atoms below T_{N2} while undergoing the ordering of the FM component (21). This can also be observed in the heat capacity measurements. Figure 4b shows the magnetic contribution to the heat capacity after subtraction of the phonon part fitted with a two terms Debye model as detailed in SI, with a negligible electronic contribution to the heat capacity. A sharp λ-type transition can be observed at T_{N1} = 88 K with a broad magnetic contribution below T_{N2} = 56 K. The calculated entropy rises up to ~140 J mol^{-1} K^{-1} at 150 K, reaching 85% of the expected theoretical value for $Mn_{11}Ta_4O_{21}$ with N = 11, S = 5/2 (for Mn^{2+}) from NRln(2S+1) (164 J mol^{-1} K^{-1}). Low temperature dielectric measurements show an increase of the capacitance under a 9 T magnetic field at T_{N2} (Figure 4c). A broad maximum is also observed in the dielectric loss (tan δ) above T_{N2}. This is in agreement with group theory: using ISOSUBGROUP with the mΓ3+ irreducible representation acting over *P*-3*c*1 and an ordered parameter direction (*a*, $a/\sqrt{3}$) (*C*2'/*c*') one can predict a proper ferroelastic and a proper ferromagnetic material (13).

In the previous part, a relation of the $Mn_{11}Ta_4O_{21}$ structure to over-stoichiometric A-site hexagonal perovskites was established as $A_{(n+1)}B_nO_{3n}$ with n = 7 and a $(cchchch)_2$ stacking sequence. The over-stoichiometry is unusual since most of the hexagonal polytypes alleviate the less-stable face-sharing octahedra motif by either metal-metal bonding (*e.g.* 4H-BaRuO_3), ordered substitution of cations with small valence (*e.g.* $Ba_4Nb_3LiO_{12}$) or via formation of B-site vacancies ($Ba_5Ta_4O_{15}$) (22). In this case, the atypical off-centering of next layer Mn in linear oligomers breaks the M-M interaction and stabilizes the structure. From a simple comparison with 14H-$BaCrO_3$ and 14H-$BaVO_3$, the interlayer separation ($c/14$) is 2.32 and 2.29 Å respectively but for $Mn_{11}Ta_4O_{21}$ it results in 2.43 Å. For the octahedrally coordinated B-site cations this larger interlayer space appears comfortable when compared with an average ionic radius from 6 $^{VI}Mn^{2+}$ and 8 $^{VI}Ta^{5+}$ layers (0.72 Å) against the smaller $^{VI}Cr^{4+}$ (0.55 Å) and $^{VI}V^{4+}$ (0.58 Å). However, for the A-site cations, the large mismatch between $^{VIII}Ba^{2+}$ (1.42 Å) *vs.* $^{VIII}Mn^{2+}$ (0.96 Å) is reduced by the insertion of an extra A-site Mn layer, and therefore the 14H octahedral skeleton holds without a strong structural modification *e.g.* as in $Ca_3Co_2O_6$-series mentioned above with $A_3A'BO_6$ general formula and A' in a trigonal prism coordination, not present in $Mn_{11}Ta_4O_{21}$. However, in terms of magnetic interactions, it is more useful to compare a polyhedral sequence build on MnO_6 octahedra. Figure 1c shows for instance a $(hhcccc)_2$ sequence with only MnO_6 octahedra, again selecting in layer heights having two MnO_6 octahedra only the less distorted

$Mn3O_6$ and $Mn5O_6$ but not $Mn4O_6$ and $Mn2O_6$. This periodic fragment has been observed in for instance 21R-$Ba_7Ca_2Mn_5O_{20}$ as $(hhcccc)_3$ (23). To see the usefulness of this alternative description, consider the $Mn_{11}Ta_4O_{21}$ magnetic structure at 60 K, shown in Figure 3b. The magnetic structure at high temperature can be thought in terms of AFM coupling between adjacent layers and with a strong frustration in Mn4 originating from the interactions with next AFM Mn1 and Mn3 layers. It can be seen that the ordered structure is mainly dictated by the B-lattice (see Table 3), i.e. Mn1 (3.2(2) μ_B), Mn3 (2.5(2) μ_B), Mn5 (3.2(2) μ_B) and Mn6 (3.2(2) μ_B), while Mn2 (1.2(2) μ_B) and Mn4 (0.0(2) μ_B) are less important. These decisive four manganese cations are the ones defining the (*hhcccc*) sequence and validate this alternative structural view. It is also interesting to consider the Mn1-Mn3-Mn1 face sharing octahedra trimer (see Figure 1c). Below T_{N1} the trimer shows solely AFM ordering i.e. ↑↓↑. This is also consistent with Goodenough-Kanamori-Andersson (GKA) rules and that strong antiferromagnetic coupling between spins is mediated by direct exchange (2.96 Å in between Mn1 – Mn3) and ~90° Mn – O – Mn links, formed by face sharing Mn1 – Mn3 – Mn1 octahedra (*h* layers). The AFM coupling along the *c* direction is explained via ~180° Mn – O – Mn super-exchange pathways formed along Mn1 – Mn5 – Mn6 – Mn6 – Mn5 – Mn1 connections (*c* layers). The AFM stacking of layers has also been observed in the whole $BaMnO_{3-\delta}$ hexagonal perovskite series (24).

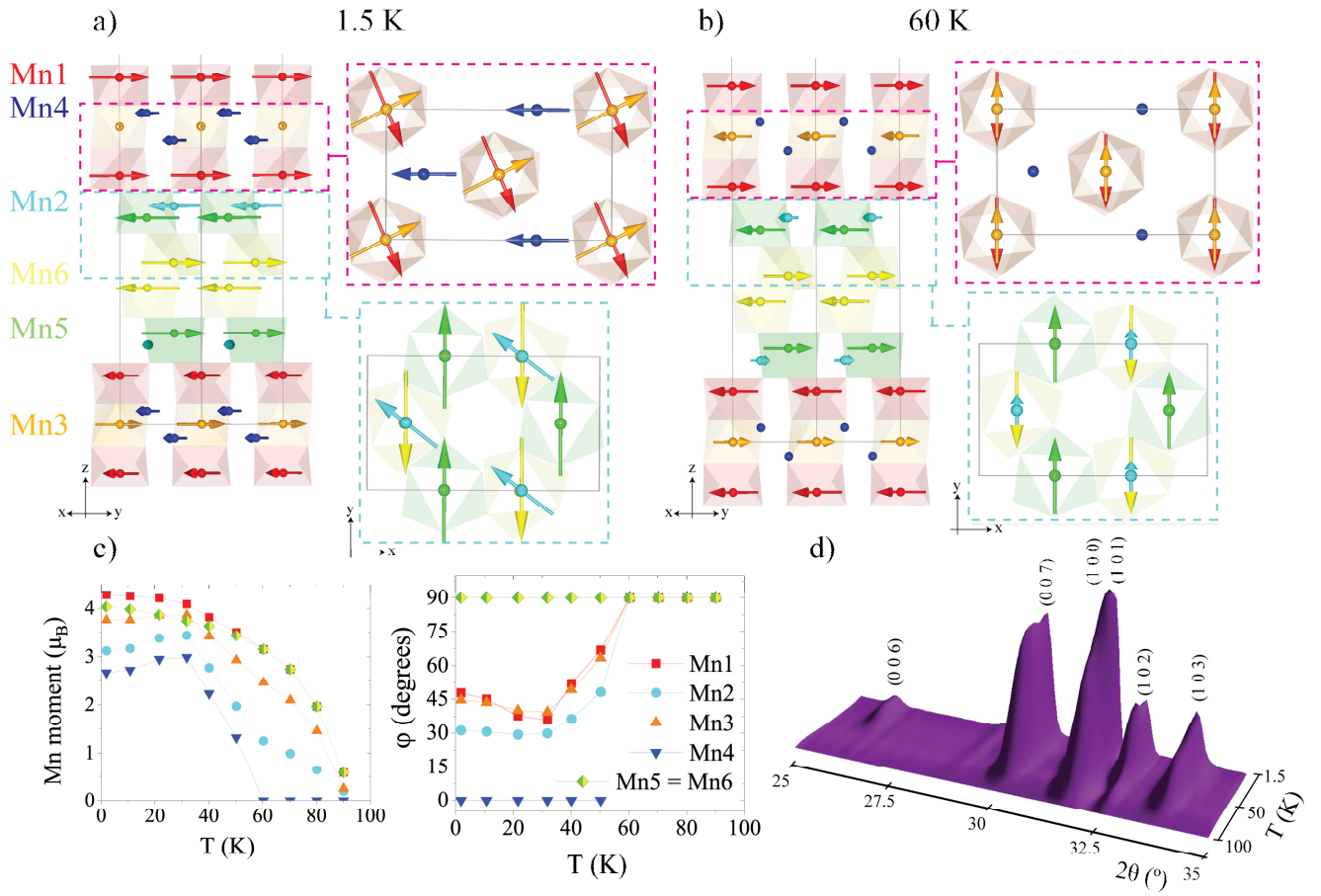

Figure 3. Magnetic structure of $Mn_{11}Ta_4O_{21}$ at 1.5 K (a) and 60 K (b). Left part shows half of the magnetic structure with different projections of the marked sections on the right. c) Thermal evolution of the Mn^{2+} magnetic moments (left) and φ angle (right). d) Temperature evolution of the most prominent magnetic maxima. Extra contribution is observed below 60 K. Colour code respects the labelling of Figure 1.

Below T_{N2}, except for Mn5 and Mn6, the Mn cations develop a m_x spin component. Mn1-Mn3-Mn1 trimer spins rotate cooperatively (→→→) against Mn4 and Mn2 (see Figure 3a right). This is a natural occurrence, Mn4 interactions with Mn1 and Mn3 are AFM and strong, therefore stay frustrated until T_{N2}. Below this temperature, Mn4 finally overcomes this frustration and orders along m_x, perpendicularly to both Mn1 and Mn3 at T_{N2}. Interestingly and promoted by Mn4 and Mn2 (A-sites), the angle between the spin directions of Mn1 and Mn3 progressively increase below T_{N2} until they become perpendicular at 2 K (±45° in successive layers).

A spin reorientation due to A-site magnetic ordering was also observed in $MnRMnSbO_6$ double-double perovskites with Mn present in both A- and B-sites (25). The strong magnetic interactions triggered below T_{N2} in $Mn_{11}Ta_4O_{21}$ are reflected in the uniaxial negative thermal expansion along the *c* axis, a broad magnetic heat capacity and a magneto-dielectric coupling as shown in Figure 4. This coupling resembles the one observed in the ordered ilmenite Mn_2InSbO_6 A-site manganite, which possesses as well a second magnetic transition that induces a spin reorientation in the *ab* plane, observed in its heat-capacity and in its magnetostriction. The expected electrical polarization of Mn_2InSbO_6 increases up to 25 % below the second magnetic transition (26). A further example of a compound having a similar behaviour is Mn_2MnWO_6 having a strong magnetostriction-polarization coupling (27). These examples show that A-site manganites appear as good playground to find new multiferroics. $Mn_{11}Ta_4O_{21}$ is centrosymmetric however any coupling of the already active mΓ3+ irrep with mΓ*i*– (*i* = 1, 2 or 3) would allow polarization in the structure and will develop magneto-electric properties. This has been demonstrated in the multiferroic cubic A-site manganite $LaMn_3Cr_4O_{12}$ with G-type magnetic orderings on A- and B-sites, which cannot explain independently the observations but only assuming a trilinear magneto-electric coupling (28,29). Similarly, structural Γ*i*– (*i* = 1, 2 or 3) degrees of freedom would also allow the magnetoelectric properties to be realised. This non-linear magnetoelectric coupling has been observed in the centrosymmetric ilmenite Mn_2FeSbO_6 (30). Moreover, $Mn_4Ta_2O_9$, also with *P-3c1* space group, shows a magnetic response under a periodic square electric pulse, *i.e.* magneto-electric properties (10). Although polarisation measurements are still needed to prove magneto-electric properties, $Mn_{11}Ta_4O_{21}$ shows a strong magneto-elastic coupling.

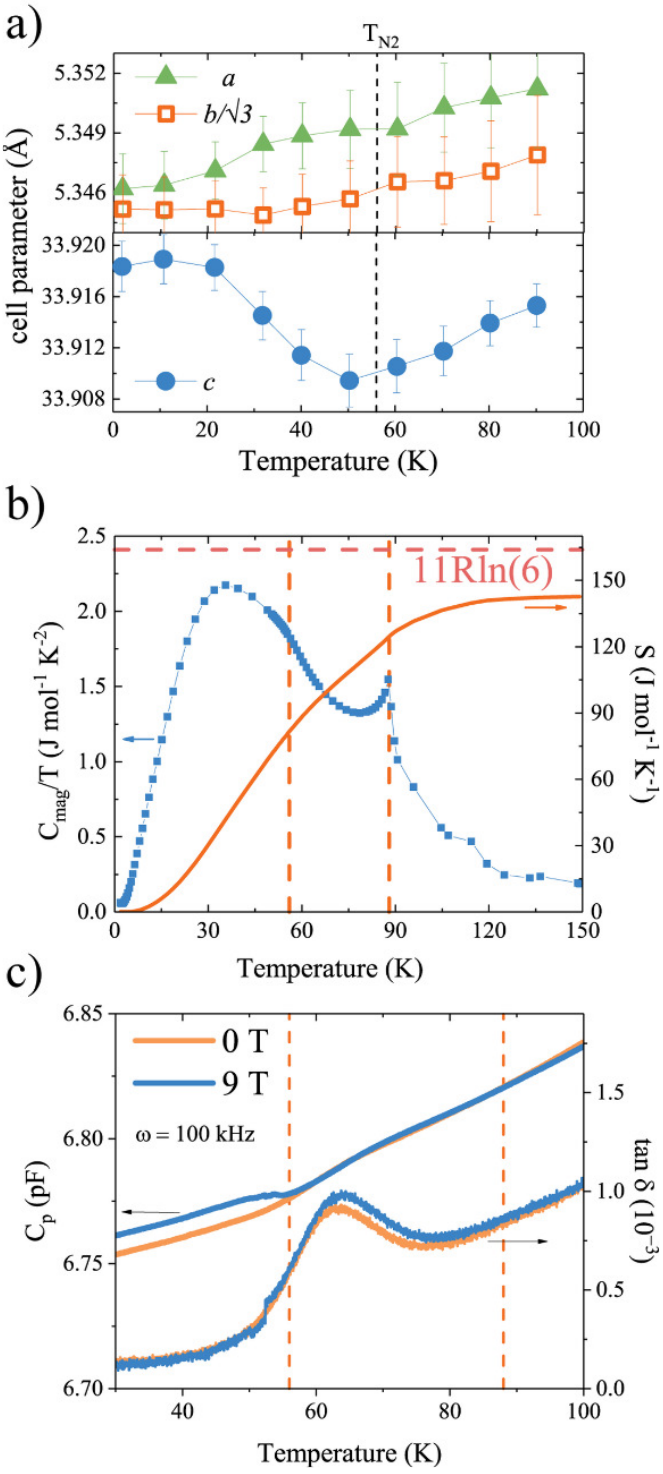

Figure 4. a) Temperature evolution of the pseudo-orthorhombic cell parameters in the magnetic state. b) Temperature dependence of $Mn_{11}Ta_4O_{21}$ magnetic specific heat divided by temperature. Calculated entropy with the ideal value for 11 Mn^{2+} as horizontal broken line. c) Thermal behaviour of the capacitance and the dielectric loss below 100 K. T_{N1} = 88 K and T_{N2} = 56 K are marked with vertical broken lines.

Conclusions

Summarizing, $Mn_{11}Ta_4O_{21}$ has been reconsidered as an over-stoichiometric hexagonal perovskite and becomes the first Hexagonal A-site Manganite. It shows a 14H – $(cchchch)_2$ sequence, previously observed only in high-pressure $BaCrO_3$ and $BaVO_3$ oxides. It presents two magnetic transitions at T_{N1} = 88 K and T_{N2} = 56 K. The high temperature magnetic structure can be easily understood if one considers a different only magnetic 14H – $(hhccccc)_2$ stacking sequence. This naturally explains the spin order in terms of direct- and super-exchange interactions following GKA rules and falling in line with all the $BaMnO_{3-\delta}$ hexagonal perovskite series. At lower temperatures a spin reorientation occurs and a ferrimagnetic component develops from the remaining A-site manganese cations. A magnetic-structural coupling is observed at T_{N2} but magneto-electric properties are yet to be proven. $Mn_{11}Ta_4O_{21}$ reveals that a new over-stoichiometric $A_{n+1}BO_{3n}$ family of hexagonal perovskites without trigonal prism coordination can be obtained and that the presence of A-site magnetic cations may demand a different structural representation in order to easily understand the magnetic behaviour.

ASSOCIATED CONTENT

Supporting Information. NPD at 60 K and heat capacity treatment. This material is available free of charge via the Internet at http://pubs.acs.org.

AUTHOR INFORMATION

Corresponding Author

* **Ángel M. Arévalo-López** – *Univ. Lille, CNRS, Centrale Lille, Univ. Artois, UMR 8181 – UCCS – Unité de Catalyse et Chimie du Solide, F-59000 Lille, France*; orcid.org/0000-0002-8745-4990;
Email: angel.arevalo-lopez@univ-lille.fr

Authors

Cintli Aguilar-Maldonado – *Univ. Lille, CNRS, Centrale Lille, Univ. Artois, UMR 8181 – UCCS – Unité de Catalyse et Chimie du Solide, F-59000 Lille, France*; orcid.org/0000-0001-7229-6216

Eugenia P. Arévalo-López – *Física Atómica y Molecular, Facultad de Ciencias, UNAM. Ciudad Universitaria, 58000, México*; orcid.org/0000-0001-5513-2623.

Clemens Ritter – *Institut Laue-Langevin, 71 Avenue des Martyrs, 32042, Grenoble Cedex, France*.

Olivier Mentré – *Univ. Lille, CNRS, Centrale Lille, Univ. Artois, UMR 8181 – UCCS – Unité de Catalyse et Chimie du Solide, F-59000 Lille, France*; orcid.org/0000-0002-1822-6003

Notes

The authors declare no competing financial interest.

ACKNOWLEDGMENTS

We thank ALBA and the ILL for beamtime provided at BL04 and D1B respectively. AMAL thanks a Marie-Słodowska Individual Fellowship in the Horizon 2020 research and innovation programme under grant agreement 750971 ("KISS ME") and the ANR-AMANTS (19-CE08-0002-01) and LOVE-ME (16-CE08-0023) projects. CAM thanks CONACyT-Mexico for a post-doctoral fellowship (CVU:350841). Chevreul Institute (FR 2638), Region Hauts-de-France, and FEDER are acknowledged for funding the X-ray diffractometers and the PPMS magnetometer.

REFERENCES

(1) Arévalo-Lopez, A. M.; Rodgers, J. A.; Senn, M. S.; Sher, F.; Farnham, J.; Gibbs, W.; Attfield, J. P. "Hard-soft" synthesis of $SrCrO_{3-\delta}$ superstructure phases. *Angew. Chem., Int. Ed.* **2012,** *51* (43), 10791-10794.

(2) Darriet, J.; Subramanian, M. A. Structural relationships between compounds based on the stacking of mixed layers related to hexagonal perovskite-type structures. *J. Mater. Chem.* **1995,** *5* (4), 543.

(3) Markkula, M.; Arevalo-Lopez, A. M.; Kusmartseva, A.; Rodgers, J. A.; Ritter, C.; Wu, H.; Attfield, J. P. Incommensurate spin order in the metallic perovskite $MnVO_3$. *Phys. Rev. B* **2011,** *84* (9), 094450.

(4) Vasala, S.; Karppinen, M. $A_2B'B''O_6$ perovskites: A review. *Prog. Solid. State Ch.* **2015,** *43* (1-2), 1-36.

(5) Arévalo-López, Á. M.; Solana-Madruga, E.; Aguilar-Maldonado, C.; Ritter, C.; Mentré, O.; Attfield, J. P. Magnetic frustration in the high-pressure Mn_2MnTeO_6 (Mn_3TeO_6-II) double perovskite. *Chem. Comm.* **2019,** *55* (96), 14470-14473.

(6) Faik, A.; Igartua, J. M.; Cuello, G. J.; Jiménez-Villacorta, F.; Castro, G. R.; Lezama, L. Crystal structures and temperature-induced phase transitions of $Sr_2Mn^{2+}W^{6+}O_6$, and of its transformation to $Sr_2Mn^{3+}W^{6+}O_{6+\delta}$. *J. Mol. Struct.* **2009,** *933* (1-3), 53-62.

(7) Tyutyunnik, A. P.; Bazuev, G. V.; Kuznetsov, M. V.; Zainulin, Y. G. Crystal structure and magnetic properties of double perovskite Mn_2FeSbO_6. *Mater. Res. Bull.* **2011,** *46* (8), 1247-1251.

(8) Rickert, K.; Pozzi, E. A.; Khanal, R.; Onoue, M.; Trimarchi, G.; Medvedeva, J. E.; Hersam, M. C.; Van Duyne, R. P.; Poeppelmeier, K. R. Selective Crystal Growth and Structural, Optical, and Electronic Studies of $Mn_3Ta_2O_8$. *Inorg. Chem.* **2015,** *54* (13), 6513-6519.

(9) Grins, J.; Esmaeilzadeh, S.; Berastegui, P.; Eriksson, S. Determination of the magnetic structure at 10 K of $Mn_3Ta_2O_8$, and refinement of the crystal structure at 295 K, using neutron powder diffraction data. *J. Mater. Chem.* **1999,** *9* (7), 1575-1578.

(10) Panja, S. N.; Manuel, P.; Nair, S. Anisotropy in the magnetization and magnetoelectric response of single crystalline $Mn_4Ta_2O_9$. **2019,** No. arXiv: 1904.10671v1, 1-7.

(11) Grins, J.; Tyutyunnik, A. Structure and Magnetic Susceptibility of $Mn_{11}Ta_4O_{21}$ and Refinement of the $Mn_4Ta_2O_9$ structure. *J Solid State Chem* **1998,** *137* (2), 276-282.

(12) Rodriguez-Carvajal, J. Recent advances in magnetic structure determination by neutron powder diffraction. *Phys. B: Condens. Matter* **1993,** *192* (1), 55-69.

(13) Stokes, H. T., Hatch, D. M. and Campbell B. J., ISODISTORT, ISOTROPY Software Suite, iso.byu.edu.

(14) Campbell, B. J.; Stokes, H. T.; Tanner, D. E.; Hatch, D. M. ISODISPLACE: A Web-Based Tool for Exploring Structural Distortions. *J. Appl. Cryst.* **2006**, *39*, 607–614.

(15) Alonso, J. A.; Martínez-Lope, M. J.; Casais, M. T.; Fernández-Díaz, M. T. Evolution of the Jahn - Teller Distortion of MnO_6 Octahedra in $RMnO_3$ Perovskites (R = Pr , Nd , Dy , Tb , Ho , Er , Y): A Neutron Diffraction Study. *Inorg. Chem.* **2000,** *39* (5), 917-923.

(16) Chamberland, B. L.; Danielson, P. S. Alkaline-earth vanadium (IV) oxides having the AVO_3 composition. *J. Solid State Chem.* **1971,** *3* (2), 243-247.

(17) Chamberland, B. L.; Katz, L. The structure of the fourteen-layer polytype of barium chromium trioxide, $BaCrO_3$. *Acta Cryst. B* **1982,** *38* (1), 54-57.

(18) El Abed, A.; Elqebbaj, S. E.; Zakhour, M.; Champeaux, M.; Perez-Mato, J. M.; Darriet, J. Crystal structure of a modulated composite structure with two subsystems: $Ba_{1.1064}CoO_3$. *J. Solid State Chem.* **2001,** *161* (2), 300-306.

(19) Ferraris, G.; Makovicky, E.; Merlino, S. *Crystallography of Modular Materials; IUCr Monographs on Crystallography, 15;* Oxford University Press: Oxford, UK., 2004.

(20) Dyer, M. S.; Collins, C.; Hodgeman, D.; Chater, P. A.; Demont, A.; Romani, S.; Sayers, R.; Thomas, M. F.; Claridge, J. B.; Darling, G. R.; Rosseinsky, M. J. Computationally assisted identification of functional inorganic materials. *Science* **2013,** *340* (6134), 847-852.

(21) Ablitt, C., Craddock, S., Senn, M.S. Mostofi, A.M.; Bristowe, N.C. The origin of uniaxial negative thermal expansion in layered perovskites. NPJ Comput. Mater. 2017, 3, 44.

(22) Mitchell, R. H. *Perovskites Modern and Ancient*; Almaz Press, **2002**.

(23) Floros, N.; Michel, C.; Hervieu, M.; Raveau, B. The n=2 Member of the New Layered Structural Family Ba5+nCa2Mn3+nO3n+14 Derived from the Hexagonal Perovskite: $Ba_7Ca_2Mn_5O_{20}$. *J. Solid State Chem.* **2002,** *168* (1), 11-17.

(24) Adkin J. J. and Hayward M. A. $BaMnO_{3-x}$ revisited: A Structural and Magnetic Study. *Chem. Mater.* **2007**, 19 (4) 755-762.

(25) Solana-Madruga, E.; Arévalo-López, Á. M.; Dos Santos-García, A. J.; Urones-Garrote, E.; Ávila-Brande, D.; Sáez-Puche, R.; Attfield, J. P. Double Double Cation Order in the High-Pressure Perovskites $MnRMnSbO_6$. *Angew. Chem., Int. Ed.* **2016,** *55* (32), 9340-9344.

(26) Arévalo-López, Á. M.; Solana-Madruga, E.; Arévalo-López, E. P.; Khalyavin, D.; Kepa, M.; Dos Santos-García, A. J.; Sáez-Puche, R.; Attfield, J. P. Evolving spin periodicity and lock-in transition in the frustrated ordered ilmenite-type β–Mn_2InSbO_6. *Phys. Rev. B* **2018,** *98* (21), 214403.

(27) Li, M.; McCabe, E. E.; Stephens, P. W.; Croft, M.; Collins, L.; Kalinin, S. V.; Deng, Z.; Retuerto, M.; Sen Gupta, A.; Padmanabhan, H.; Gopalan, V.; Grams, C. P.; Hemberger, J.; Orlandi, F.; Manuel, P.; Li, W.; Jin, C.; Walker, D.; Greenblatt, M. Magnetostriction-polarization coupling in multiferroic Mn_2MnWO_6. *Nat. Commun.* **2017,** *8* (1), 2037.

(28) Wang, X.; Chai, Y.; Zhou, L.; Cao, H.; Cruz, C. D.; Yang, J.; Dai, J.; Yin, Y.; Yuan, Z.; Zhang, S.; Yu, R.; Azuma, M.; Shimakawa, Y.; Zhang, H.; Dong, S.; Sun, Y.; Jin, C.; Long, Y. Observation of Magnetoelectric Multiferroicity in a Cubic Perovskite System: $LaMn_3Cr_4O_{12}$. *Phys. Rev. Lett.* **2015,** *115* (8), 1-5.

(29) Senn, M. S.; Bristowe, N. C. A group-theoretical approach to enumerating magnetoelectric and multiferroic couplings in perovskites. *Acta Cryst. A* **2018,** *74* (4), 308-321.

(30) Dos santos-García, A. J.; Solana-Madruga, E.; Ritter, C.; Andrada-Chacón, A.; Sánchez-Benítez, J.; Mompean, F. J.; Garcia-Hernandez, M.; Sáez-Puche, R.; Schmidt, R. Large Magnetoelectric Coupling Near Room Temperature in Synthetic Melanostibite Mn_2FeSbO_6. *Angew. Chem., Int. Ed.* **2017,** *56* (16), 4438-4442.

"For Table of Contents Only"

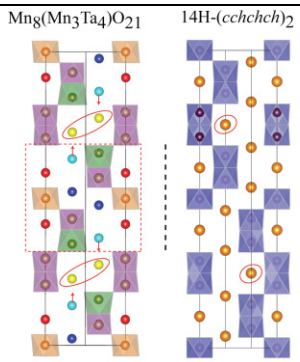

$Mn_{11}Ta_4O_{21}$ structure is presented as an hexagonal A-site manganite. It shows two magnetic transitions that belong to the same mΓ3+ irrep with a strong magneto-elastic coupling.